

Noble gas films on a decagonal AlNiCo quasicrystal

W Setyawan¹, R D Diehl², N Ferralis³, M W Cole² and S Curtarolo¹

¹ Department of Mechanical Engineering and Materials Science, Duke University, Durham, NC 27708

² Department of Physics and Materials Research Institute, Penn State University, University Park, PA 16801

³ Department of Chemical Engineering, University of California, Berkeley, CA 94720

E-mail: stefano@duke.edu

Abstract. Thermodynamic properties of Ne, Ar, Kr, and Xe adsorbed on an Al-Ni-Co quasicrystalline surface (QC) are studied with Grand Canonical Monte Carlo by employing Lennard-Jones interactions with parameter values derived from experiments and traditional combining rules. In all the gas/QC systems, a layer-by-layer film growth is observed at low temperature. The monolayers have regular epitaxial fivefold arrangements which evolve toward sixfold close-packed structures as the pressure is increased. The final states can contain considerable or negligible amounts of defects. In the latter case, there occurs a structural transition from five to sixfold symmetry which can be described by introducing an order parameter, whose evolution characterizes the transition to be continuous or discontinuous as in the case of Xe/QC (first-order transition with associated latent heat). By simulating fictitious noble gases, we find that the existence of the transition is correlated with the size mismatch between adsorbate and substrate's characteristic lengths. A simple rule is proposed to predict the phenomenon.

1. Introduction

A tremendous interest in surface structures and phase transitions grew out of the fact that surface systems are ideal for exploring the effects of competing interactions [1, 2]. A form of competing interactions seen in adsorption involves either a length scale or a symmetry mismatch between the adsorbate-adsorbate interaction and the adsorbate-substrate interaction [3, 4]. Some consequences of such mismatches include density modulations [5, 6], domain walls [7], epitaxial rotation in the adsorbed layer [8, 9, 10, 11, 12, 13], and a disruption of the normal periodicity and growth in the film [14, 15, 16]. Domain wall systems in monolayers can be thought of as some of the first examples of ordering at the nanoscale, where the length scale is defined by the lattice mismatch, and interestingly, mismatched systems are now designed and used for growing nanostructure arrays having specific symmetries and spacings.

After the discovery of quasicrystals, an interest grew in the possibility of using quasicrystal surfaces as substrates to grow quasicrystalline films of a single element,

which do not occur in nature [17]. Such a system necessarily has a lattice mismatch between the adsorbate and the substrate, and the effects are seen in the diverse examples of film structures and growth modes that occur for these systems [14, 15, 16, 18, 19, 20, 21]. There is now interest in being able to design and produce quasiperiodic arrays of nanoclusters on quasicrystal surfaces, but the complex interactions involved in the adsorbate-substrate interactions make it difficult to design specific nanostructures.

Recently, our group has begun to explore the behavior of simple gases physisorbed on quasicrystalline surfaces [22, 23, 24, 25]. The key questions motivating these studies are analogous to those for periodic substrates; for example, what are the energy scales of the adsorbed film and what is the resulting structure of the film? The latter problem includes a specific question: under what conditions, if any, of temperature (T) and vapor pressure (P) does the film form an epitaxial phase on the surface and when does it form an alternative structure, a hexagonal, close-packed array of atoms or molecules (i.e., the film's ground state within the 2D approximation). One expects the low P , submonolayer behavior to be that of a film conforming to the substrate, attracted to the sites offering the highest binding energies. The hypothetical behavior at high P includes several possibilities, e.g. bulk-like film growth, amorphous structures, island formation or the absence of any multilayer film. Which of these scenarios (or others) actually occurs is a function of the gas-surface and gas-gas interactions.

In this article, we report the results of Grand Canonical Monte Carlo (GCMC) [26, 27] simulations of Ne, Ar, Kr, and Xe adsorbed on the tenfold surface of a decagonal $\text{Al}_{73}\text{Ni}_{10}\text{Co}_{17}$ quasicrystal [28, 29]. We organize our article as follows. In Section 2 we discuss briefly the method. Section 3 is devoted to the results of Ne, Ar, Kr, and Xe adsorbed on the AlNiCo. In Section 4 we compare the results of all gases. Section 5 contains conclusions and comments on strategies for future research in this area.

2. Method

By using the Grand Canonical Monte Carlo (GCMC) simulation method [2, 26, 27] we study the adsorption of noble gases: Ne, Ar, Kr, and Xe on the tenfold surface of a decagonal $\text{Al}_{73}\text{Ni}_{10}\text{Co}_{17}$ quasicrystal [28, 29] (He is omitted because it requires a quantum treatment). In this article, we use the abbreviation QC to refer to this particular quasicrystalline substrate. GCMC, a widely used method, is described in detail in references [23, 24, 25, 30]. Only a brief overview is given here.

2.1. Grand Canonical Monte Carlo

At constant temperature, T , and volume, V , the GCMC method explores the configurational phase space using the Metropolis algorithm and finds the equilibrium number of adsorbed atoms (adatoms), N , as a function of the chemical potential, μ , of the gas. The adsorbed atoms are in equilibrium with the coexisting gas: the chemical potential of the gas is constant throughout the system. In addition, the coexisting gas

is taken to be ideal. With this method we determine adsorption isotherms, ρ_N , and density profiles, $\rho(x, y)$, as a function of the pressure, $P(T, \mu)$. For each data point in an isotherm, we perform at least 18 million GCMC steps to reach equilibrium. Each step is an attempted displacement, creation, or deletion of an atom with execution probabilities equal to 0.2, 0.4, and 0.4, respectively [24, 25, 30]. At least 27 million steps are performed in the subsequent data-gathering and -averaging phase.

2.2. Unit cell

The unit cell is tetragonal. We take a square section of the surface, A , of side 5.12 nm, to be the (x, y) part of the unit cell in the simulation, for which we assume periodic boundary conditions along the basal directions. Although this assumption limits the accuracy of the long range QC structure, it is numerically necessary for these simulations. Since the size of the cell is relatively large compared to that of the noble gases, the cell is accurately representative of order on short-to-moderate length scales. A hard wall at 10 nm above the surface along z is used to confine the coexisting vapor phase. The simulation results for Xe over QC, presented below, are consistent with both our results from experiments [31] and virial calculations [32]. Hence, the calculations may also be accurate for other systems.

2.3. Gas-gas and gas-surface interactions

The gas-gas potentials are taken to be Lennard-Jones (LJ) 12-6 interactions, with the parameter values ϵ_{gg} and σ_{gg} listed in table 1. The gas-surface potentials are based on a summation of two-body interactions between the gas and the individual constituent atoms of the substrate: Al, Ni and Co [22, 28, 32]. The gas-surface pair interactions are also assumed to have LJ form, with parameter values taken from traditional combining rules, using atomic sizes derived from bulk crystalline lattice constants [31, 32, 33, 34]. The LJ gas-surface parameters are ϵ_{gas-Al} and σ_{gas-Al} for Al, and ϵ_{gas-TM} and σ_{gas-TM} for the two transition metals Ni and Co. All these values are listed in the upper part of table 1. In the calculation of the adsorption potential, we assume a structure of the unrelaxed surface taken from the empirical fit to LEED data [29].

2.4. Adsorption potentials

Figures 1(a), 1(c), 1(e), and 1(g) show the function $V_{min}(x, y)$ of Ne, Ar, Kr, and Xe on the QC, respectively, which is calculated by minimizing the adsorption potentials, $V(x, y, z)$, along the z direction at every value of the coordinates (x, y) :

$$V_{min}(x, y) \equiv \min \{V(x, y, z)\}|_{\text{along } z}. \quad (1)$$

The figures reveal the fivefold rotational symmetry of the substrate. Dark spots correspond to the most attractive regions of the substrate. By choosing appropriate sets of five dark spots, we can identify pentagons, whose sizes follow the inflationary

Table 1. Parameter values for the 12-6 Lennard-Jones interactions. TM is the label for Ni or Co.

	ϵ_{gg} (meV)	σ_{gg} (nm)	ϵ_{gas-Al} (meV)	σ_{gas-Al} (nm)	ϵ_{gas-TM} (meV)	σ_{gas-TM} (nm)
Ne	2.92	0.278	9.40	0.264	9.01	0.249
Ar	10.32	0.340	17.67	0.295	16.93	0.280
Kr	14.73	0.360	21.11	0.305	20.23	0.290
Xe	19.04	0.410	24.00	0.330	23.00	0.315
iNe ⁽¹⁾	2.92	0.410	5.45	0.330	5.22	0.315
dXe ⁽¹⁾	19.04	0.278	41.39	0.264	39.67	0.249
dXe ⁽²⁾	19.04	0.390	25.88	0.320	24.80	0.305
iXe ⁽¹⁾	19.04	0.550	14.96	0.400	14.34	0.385
iXe ⁽²⁾	19.04	0.675	10.52	0.462	10.08	0.447

property of the QC. Note the pentagon at the center of each figure: it will be used to extract the geometrical parameters λ_s and λ_c in Section 4.

To characterize the corrugation, not well-defined for aperiodic surfaces, we calculate the distribution function $f(V_{min})$, the average $\langle V_{min} \rangle$ and standard deviation SD of $V_{min}(x, y)$ as:

$$f(V_{min})dV_{min} \equiv \text{probability} \left\{ V_{min} \in [V_{min}, V_{min} + dV_{min}] \right\} \quad (2)$$

$$\langle V_{min} \rangle \equiv \int_{-\infty}^{\infty} f(V_{min})V_{min} dV_{min}, \quad (3)$$

$$SD^2 \equiv \int_{-\infty}^{\infty} f(V_{min})(V_{min} - \langle V_{min} \rangle)^2 dV_{min}. \quad (4)$$

Figures 1(b), 1(d), 1(f), and 1(h) show $f(V_{min})$ of the adsorption potential for Ne, Ar, Kr, and Xe on the QC, respectively. $V_{min}(x, y)$ extends by more than 2·SD around its average, revealing the high corrugation of the gas-surface interaction in these four systems. The average and SD of $V_{min}(x, y)$ for these systems are listed in the upper part of table 2.

2.5. Effective parameters

For every gas-surface interaction we define two effective parameters σ_{gs} and D_{gs} . σ_{gs} represents the averaged LJ size parameter of the interaction, calculated following the traditional combining rules [33]:

$$\sigma_{gs} \equiv x_{Al}\sigma_{g-Al} + x_{Ni}\sigma_{g-Ni} + x_{Co}\sigma_{g-Co}, \quad (5)$$

where x_{Al} , x_{Ni} , and x_{Co} are the concentrations of Al, Ni, and Co in the QC, respectively. D_{gs} represents the well depth of the laterally averaged potential $V(z)$:

$$D_{gs} \equiv -\min \{V(z)\}|_{\text{along } z}. \quad (6)$$

In addition, we normalize the σ_{gs} and D_{gs} with respect to the gas-gas interactions:

$$\sigma_{gs}^* \equiv \sigma_{gs}/\sigma_{gg}, \quad (7)$$

$$D_{gs}^* \equiv D_{gs}/\epsilon_{gg}. \quad (8)$$

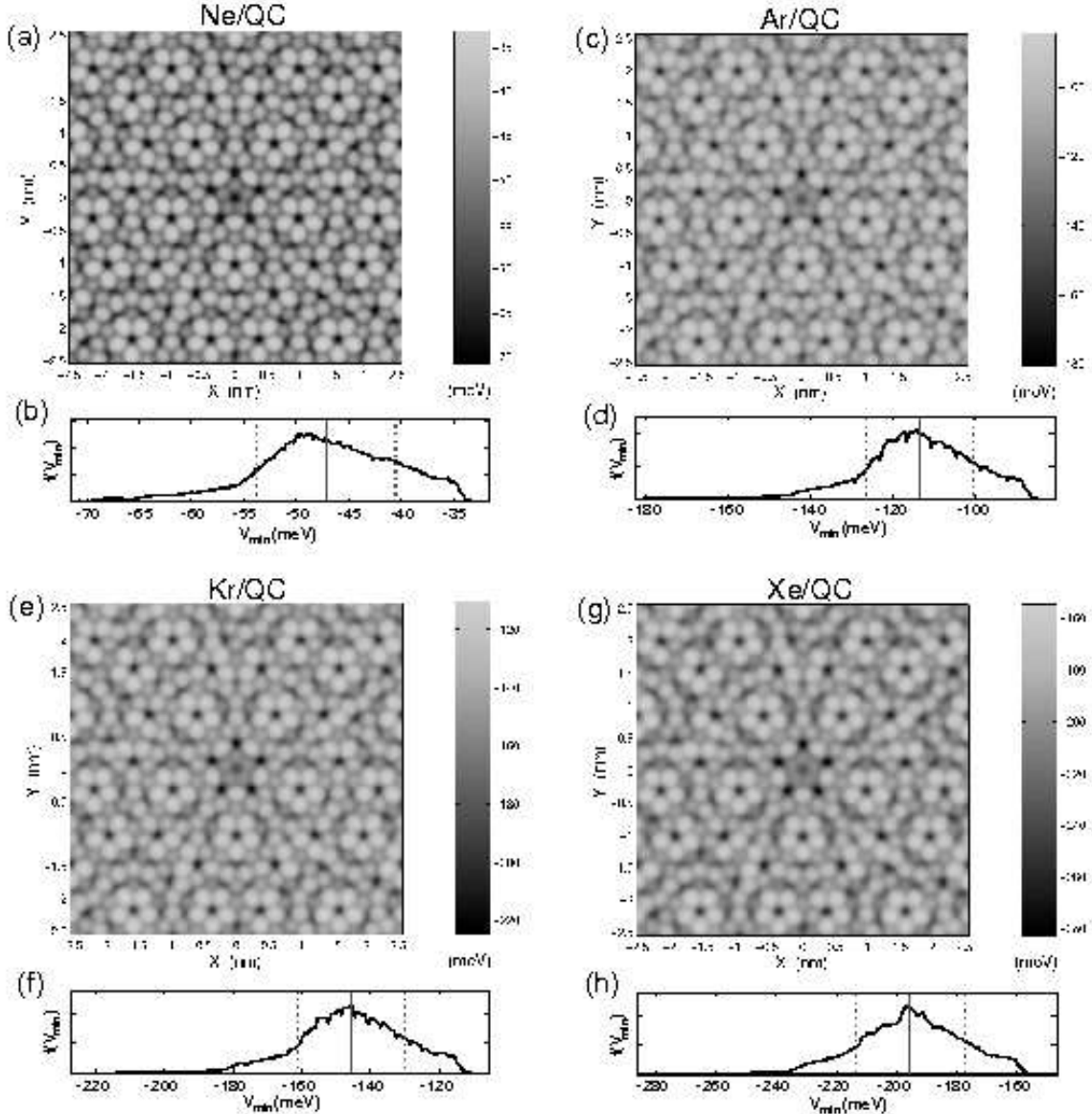


Figure 1. (color online). Computed adsorption potentials for (a) Ne, (c) Ar, (e) Kr, and (g) Xe on the quasicrystal, obtained by minimizing $V(x, y, z)$ with respect to z . The distribution of the minimum value of these potentials is plotted in (b, d, f, and h) respectively: the solid line marks the average value $\langle V_{min} \rangle$, the dashed lines mark the values at $\langle V_{min} \rangle \pm SD$.

The values of the effective parameters σ_{gs} , D_{gs} , σ_{gs}^* , and D_{gs}^* for the four gas-surface interactions are listed in the upper part of table 2. We also include the well depth for Ne, Ar, Kr, and Xe on graphite, as comparison [35].

2.6. Fictitious gases

As shown in tables 1 and 2, Ne is the *smallest* atom and has the *weakest* gas-gas and gas-surface interactions (minima of σ_{gg} , σ_{gs} , ϵ_{gg} and D_{gs}). In addition, Xe is the *largest*

Table 2. Range, average ($\langle V_{min} \rangle$), and standard deviation (SD) of the interaction $V_{min}(x,y)$ on the QC. Effective parameters of the gas-surface interactions (D_{gs} , σ_{gs} , D_{gs}^* , σ_{gs}^*), and, for comparison, the best estimated well depths D_{gs}^{Gr} on graphite [35].

	V_{min} range (meV)	$\langle V_{min} \rangle$ (meV)	SD (meV)	D_{gs} (meV)	σ_{gs} (nm)	D_{gs}^* (D_{gs}/ϵ_{gg})	σ_{gs}^* (σ_{gs}/σ_{gg})	D_{gs}^{Gr} (meV)
Ne	-71 to -33	-47.43	6.63	43.89	0.260	15.03	0.935	33
Ar	-181 to -85	-113.32	13.06	108.37	0.291	10.50	0.856	96
Kr	-225 to -111	-145.71	15.68	140.18	0.301	9.52	0.836	125
Xe	-283 to -155	-195.46	17.93	193.25	0.326	10.15	0.795	162
iNe ⁽¹⁾	-65 to -36	-45.11	4.08	43.89	0.326	15.03	0.795	
dXe ⁽¹⁾	-305 to -150	-207.55	29.18	193.25	0.260	10.15	0.935	
dXe ⁽²⁾	-295 to -155	-199.40	19.33	193.25	0.316	10.15	0.810	
iXe ⁽¹⁾	-248 to -170	-195.31	11.21	193.25	0.396	10.15	0.720	
iXe ⁽²⁾	-230 to -180	-194.25	7.77	193.25	0.458	10.15	0.679	

atom and has the *strongest* gas-gas and gas-surface interactions (maxima of σ_{gg} , σ_{gs} , ϵ_{gg} and D_{gs}). Therefore, for our analysis, it is useful to consider two “fictitious” gases, iNe⁽¹⁾ and dXe⁽¹⁾, which are combinations of Ne and Xe parameters.

iNe⁽¹⁾ represents an “inflated” version of Ne, having the same gas-gas and average gas-surface interactions of Ne but the geometrical dimensions of Xe:

$$\{\epsilon_{gg}, D_{gs}, D_{gs}^*\}[iNe^{(1)}] \equiv \{\epsilon_{gg}, D_{gs}, D_{gs}^*\}[Ne], \quad (9)$$

$$\{\sigma_{gg}, \sigma_{gs}, \sigma_{gs}^*\}[iNe^{(1)}] \equiv \{\sigma_{gg}, \sigma_{gs}, \sigma_{gs}^*\}[Xe]. \quad (10)$$

dXe⁽¹⁾ represents a “deflated” version of Xe, having the same gas-gas and average gas-surface interactions of Xe but the geometrical dimensions of Ne:

$$\{\epsilon_{gg}, D_{gs}, D_{gs}^*\}[dXe^{(1)}] \equiv \{\epsilon_{gg}, D_{gs}, D_{gs}^*\}[Xe], \quad (11)$$

$$\{\sigma_{gg}, \sigma_{gs}, \sigma_{gs}^*\}[dXe^{(1)}] \equiv \{\sigma_{gg}, \sigma_{gs}, \sigma_{gs}^*\}[Ne]. \quad (12)$$

The resulting LJ parameters for iNe⁽¹⁾ and dXe⁽¹⁾ are summarized in the central parts of tables 1 and 2. Furthermore, we also define three other fictitious versions of Xe: dXe⁽²⁾, iXe⁽¹⁾, and iXe⁽²⁾ which have the same gas-gas and average gas-surface interactions of Xe but deflated or inflated geometrical parameters. The last three fictitious gases will be used in Section 4. The LJ parameters for these gases are summarized in the lower parts of tables 1 and 2. In simulating fictitious gases, we implicitly rescale the substrate’s strengths so that the resulting adsorption potentials have the same D_{gs} as the non-inflated or non-deflated ones (equations 9 and 11).

2.7. Chemical potential, order parameter, and ordering transition

To appropriately characterize the evolution of the adsorption processes of the gases we define a *reduced chemical potential* μ^* , as:

$$\mu^* \equiv \frac{\mu - \mu_1}{\mu_2 - \mu_1}, \quad (13)$$

where μ_1 and μ_2 are the chemical potentials at the onset of the first and second layer formation, respectively. In addition, as done in reference [24, 25], we introduce the *order*

parameter ρ_{5-6} , defined as the probability of existence of fivefold defect:

$$\rho_{5-6} \equiv \frac{N_5}{N_5 + N_6}, \quad (14)$$

where N_5 and N_6 are the numbers of atoms having 2D coordination equal to 5 and 6, respectively. The 2D coordination is the number of neighboring atoms within a cutoff radius of $a_{NN} \cdot 1.366$ where a_{NN} is the first nearest neighbor (NN) distance of the gas in the solid phase and $1.366 = \cos(\pi/6) + 1/2$ is the average of the first and the second NN distances in a triangular lattice.

In a fivefold ordering, most arrangements are hollow or filled pentagons with atoms having mostly five neighbors. Hence, the particular choice of ρ_{5-6} is motivated by the fact that such pentagons can become hexagons by gaining additional atoms with five or six neighbors. **Definition:** the five to sixfold ordering transition is defined as a decrease of the order parameter to a small or negligible final value. The phenomenon can be abrupt (first-order) or continuous. Within this framework, ρ_{5-6} and $(1 - \rho_{5-6})$ can be considered as the fractions of pentagonal and triangular phases in the film, respectively.

3. RESULTS

3.1. Adsorption isotherms

Figure 2 shows the adsorption isotherms of Ne, Ar, Kr, and Xe on the QC. The plotted quantities are the densities of adatoms per unit area, ρ_N , as a function of pressure at various temperatures. The simulated ranges and the experimental triple point temperatures (T_t) for Ne, Ar, Kr, and Xe are listed in table 3. A layer-by-layer film growth is visible at low temperatures. A complete wetting behavior is observed as indicated by a continuous film growth at temperatures above T_t (isotherms at $T > T_t$ are shown as dotted curves). This behavior, observed in spite of the high corrugation, is interesting as corrugation has been shown to be capable of preventing wetting [36, 37].

Although vertical steps corresponding to layers' formation are evident in the isotherms, the slopes of the isotherms' plateaus at the same normalized temperatures ($T^* \equiv T/\epsilon_{gg} = 0.35$) differ between systems. To characterize this, we calculate the increase of each layer density, $\Delta\rho_N$, from the formation to the onset of the subsequent layer. $\Delta\rho_N$ is defined as $\Delta\rho_N \equiv (\rho_B - \rho_A)/\rho_A$ and the values are reported in table 3 (points (A) and (B) are specified in figure 2). We observe that, as the size of noble gas increases $\Delta\rho_N$ become smaller, indicating that the substrate corrugation has a more pronounced effect on smaller adsorbates, as expected since they penetrate deeper into the corrugation pockets. However, Xe/QC does not follow this trend. This arises from the complex interplay between the corrugation energy and length of the potential with respect to the parameters of the gas ($\sigma_{gg}, \epsilon_{gg}$) in determining the density of the adsorbed layers. In the case of Ne, Ar, and Kr on QC, the densities at points (A) are approximately the same ($\rho_A = 5.4 \text{ atoms/nm}^2$), whereas that of Xe/QC is considerably

smaller ($\rho_A = 4.2$ atoms/nm²), because the Xe dimension σ_{gg} becomes comparable to the characteristic length (corrugation) of the potential. This effect is clarified by the density profile of the films, $\rho(x, y)$, shown in figures 3 and 4. As can be seen at points (A), the density profiles of Ne, Ar, and Kr on QC are the same, i.e. the same set of dark spots appear in their plots. For Xe, some spots are separated with distances smaller than its core radius (σ_{gg}), causing repulsive interactions. Hence these spots will not likely appear in the density profile, resulting in a lower ρ_A . More discussion on how interaction parameters affect the shape of the isotherms is presented in Section 4. Note that the second layer in each system has a smaller $\Delta\rho_N$ than the first one. The explanation will be given when we discuss the evolution of density profiles.

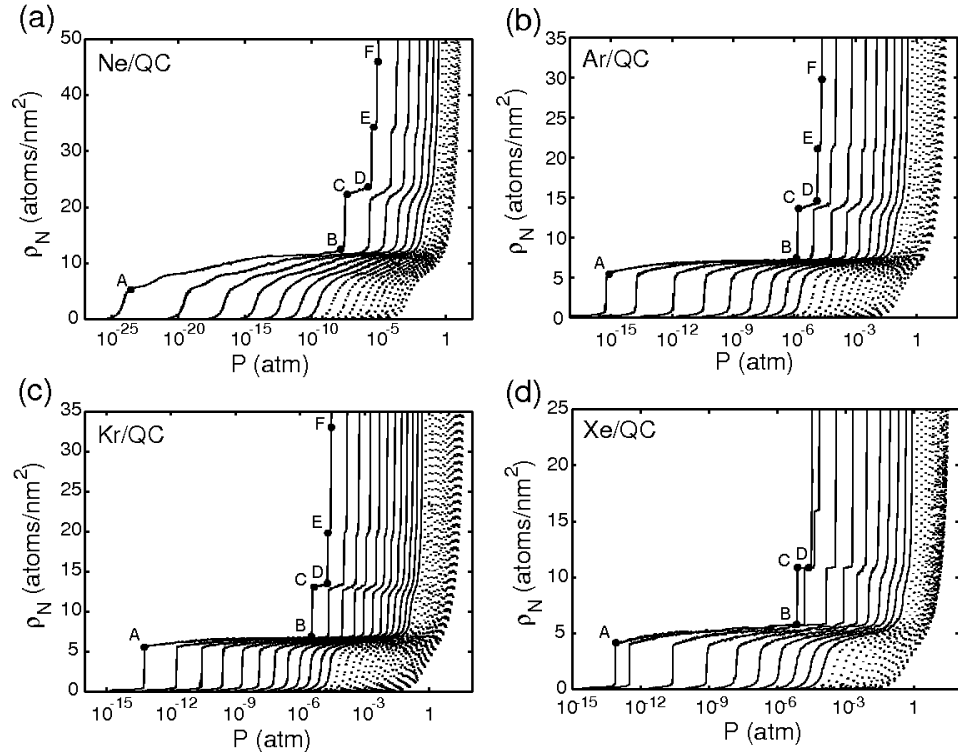


Figure 2. Computed adsorption isotherms for all the gas/QC systems. The ranges of temperatures under study are: Ne: $T = 14$ K to 46 K in 2 K steps, Ar: 45 K to 155 K in 5 K steps, Kr: 65 K to 225 K in 5 K steps, Xe: 80 K to 280 K in 10 K steps. Additional isotherms are shown with solid circles at $T^* = 0.35$: $T = 11.8$ K (Ne), $T = 41.7$ K (Ar), $T = 59.6$ K (Kr), and $T = 77$ K (Xe). Isotherms above the triple point temperatures are shown as dotted curves.

3.2. Density profiles

Figures 3 and 4 show the density profiles $\rho(x, y)$ at $T^* = 0.35$ for the outer layers of Ne, Ar, Kr, and Xe adsorbed on the QC at the pressures corresponding to points (A) through (F) of the isotherms in figure 2.

Table 3. Results for Ne, Ar, Kr, and Xe adsorbed on the QC. T_t is taken from reference[38]. The density increase ($\Delta\rho_N$) in the first and second layers is calculated at $T^* = 0.35$ from point (A) to (B) and (C) to (D) in figure 2, respectively.

	simulated T (K)	$T^* \equiv T/\epsilon_{gg}$	T_t (K)	$\Delta\rho_N$ at $T^* = 0.35$ for 1 st layer	$\Delta\rho_N$ at $T^* = 0.35$ for 2 nd layer	θ_r
Ne	11.8 → 46	0.35 → 1.36	24.55	(12.2-5.3)/5.3=1.30	(11.1-10.2)/10.2=0.09	6°
Ar	41.7 → 155	0.35 → 1.29	83.81	(7.3-5.5)/5.5=0.33	(6.9-6.4)/6.4=0.08	30°
Kr	59.6 → 225	0.35 → 1.32	115.76	(6.9-5.5)/5.5=0.25	(6.6-6.3)/6.3=0.05	42°
Xe	77 → 280	0.35 → 1.27	161.39	(5.8-4.2)/4.2=0.38	(5.2-5.2)/5.2=0	54°

Ne/QC system. Figure 3(a) shows the evolution of adsorbed Ne. At the formation of the first layer, adatoms are arranged in a pentagonal manner following the order of the substrate, as shown by the discrete spots of the Fourier transform (FT) having tenfold symmetry (point (A)). As the pressure increases, the arrangement gradually loses its pentagonal character. In fact, at point (B) the adatoms are arranged in patches of triangular lattices and the FT consists of uniformly-spaced concentric rings with hexagonal resemblance. The absence of long-range ordering in the density profile is indicated by the lack of discrete spots in the FT. This behavior persists throughout the formation of the second layer (points (C) and (D)) until the appearance of the third layer (point (E)). At this and higher pressures, the FT shows patterns oriented as hexagons rotated by $\theta_r = 6^\circ$, indicating the presence of short-range triangular order on the outer layer (point (F)). In summary, between points (A) and (F) the arrangement evolves from pentagonal fivefold to triangular sixfold with considerable disorder, as the upper part of the density profile at point (F) shows. The transformation of the density profile, from a lower-packing-density (pentagonal) to a higher-packing-density structure (irregular triangular), occurs mostly in the monolayer from points (A) to (B), causing the largest density increase of the first layer with respect to that of the other layers (see the end of Section 3.2 for more discussion). Due to the considerable amount of disorder in the final state Ne/QC does not satisfy the requirements for the transition as defined in Section 2.7.

Ar/QC and Kr/QC systems. Figures 3(b) and 4(a) show the evolutions of Ar/QC and Kr/QC: they are similar to the Ne/QC system. For Ar/QC, the pentagonal structure at the formation of the first layer is confirmed by the FT showing discrete spots having tenfold symmetry (point (A)). The quasicrystal symmetry strongly affects the overlayers' structures up to the third layer by preventing the adatoms from forming a triangular lattice (point (E)). This appears, finally, in the lower part of the density profile at the formation of the fourth layer as confirmed by the FT showing discrete spots with sixfold symmetry (point (F)). Similarly to the Ne/QC system, disorder does not disappear but remain present in the middle of the density profile corresponding to the highest coverage before saturation (point (F)). Similar situation occurs also for the evolution of Kr/QC as shown in figure 4(a).

Xe/QC system. Figure 4(b) shows the evolution of adsorbed Xe. At the formation of the first layer, adatoms are arranged in a fivefold ordering similar to that

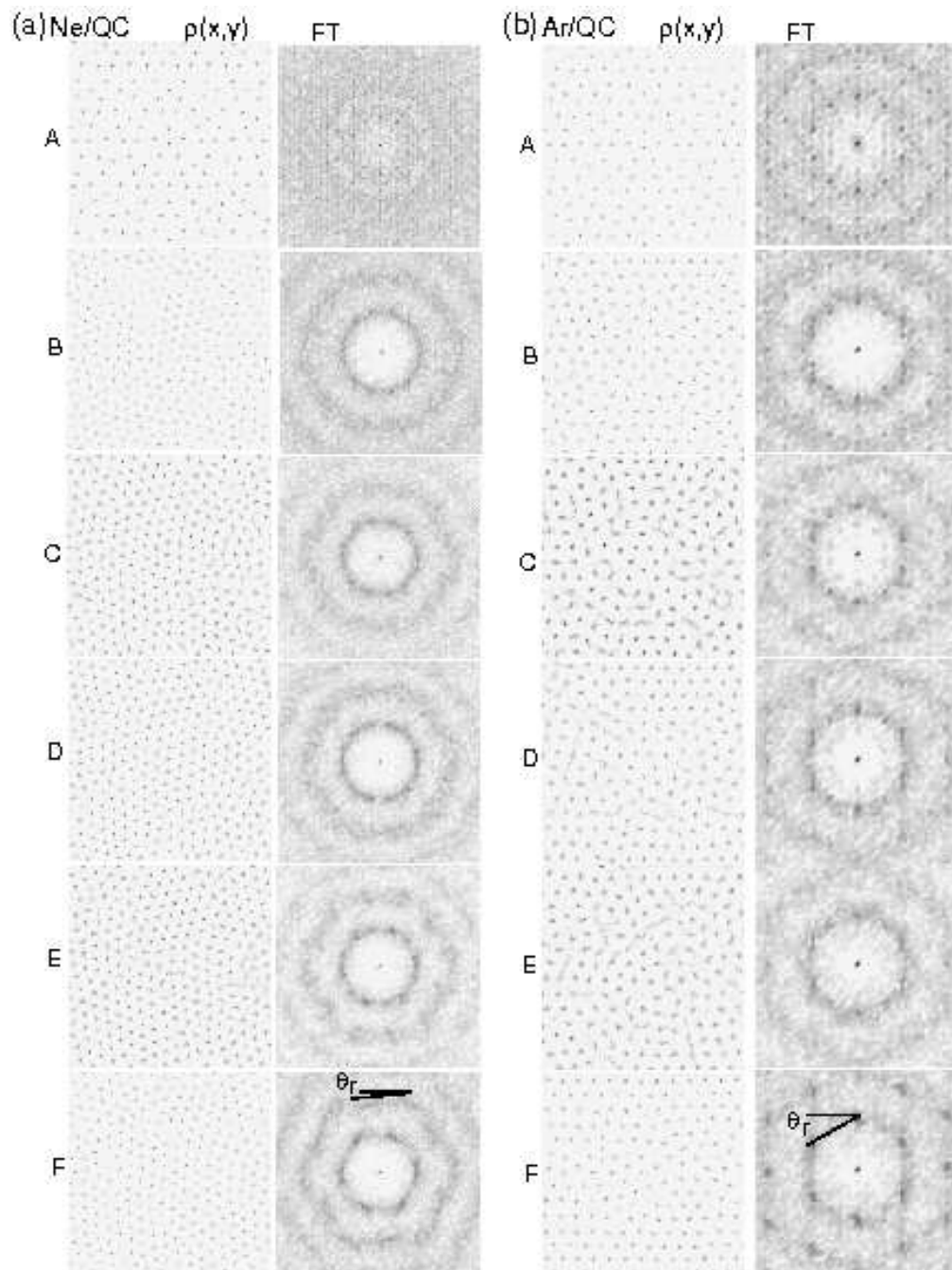


Figure 3. Density profiles and Fourier transforms of the outer layer at $T^* = 0.35$ for Ne/QC ($T = 11.8$ K) and Ar/QC ($T = 41.7$ K), corresponding to points (A) through (F) of figure 2.

of the substrate as shown by the discrete spots of the FT having tenfold symmetry (point (A)). At point (B), the density profile shows a well-defined triangular lattice not present in the other three systems: the FT shows discrete spots arranged in regular and equally-spaced concentric hexagons with the smallest containing six clear spots. Thus, at point (B) and at higher pressures, the Xe overlayers can be considered to have a regular closed-packed structure with negligible irregularities.

It is interesting to compare the orientation of the hexagons on FT for these four adsorbed gases at the highest available pressures before saturation (point (F) for Ne, Ar, and Kr, and point (D) for Xe). We define the orientation angles as the smallest of the possible clockwise rotations to be applied to the hexagons to obtain one side horizontal, as shown in figures 3 and 4. Such angles are $\theta_r = 6^\circ, 30^\circ, 42^\circ$, and 54° , for adsorbed Ne, Ar, Kr, and Xe, respectively. These orientations, induced by the fivefold symmetry of the QC, can differ only by multiples of $n \cdot 12^\circ$ [24, 25]. Since hexagons have sixfold symmetry, our systems can access only five possible orientations ($6, 18, 30, 42, 54^\circ$), and the final angles are determined by the interplay between the adsorbate solid phase lattice spacing, the periodic simulation cell size, and the potential corrugation. For systems without periodic boundary conditions, the ground state has been found to be fivefold degenerate, as should be the case [24, 25].

In every system, the increase of the density for each layer is strongly correlated to the commensurability with its support: the more similar they are, the more flat the adsorption isotherm will be (note that the support for the $(N+1)^{th}$ -layer is the N^{th} -layer). For example, the Xe/QC system has an almost perfect hexagonal structure at point (B) (due to its first-order five to sixfold ordering transition as described in the next section). Hence, all the further overlayers growing on the top of the monolayer will be at least “*as regular*” as the first layer, and have the negligible density increase as listed in table 3.

3.3. Order parameters

The evolution of the order parameter ρ_{5-6} is shown in figure 5 as a function of the normalized chemical potential, μ^* , at $T^*=0.35$ for all the noble gases/QC systems.

Ne/QC, Ar/QC, and Kr/QC systems. The ρ_{5-6} plots for the first four layers observed before bulk condensation are shown in panels (a)–(c). As the chemical potential μ^* increases, ρ_{5-6} decreases continuously reaching a constant value only for Kr/QC. At bulk condensation, the values of ρ_{5-6} are still high, approximately $0.35 \sim 0.45$. Data at higher temperatures shows a similar behavior (up to $T=24$ K ($T^*=0.71$) for Ne, $T=70$ K ($T^*=0.58$) for Ar, and $T=90$ K ($T^*=0.53$) for Kr). Thus, we conclude that these systems do not undergo the ordering transition.

Xe/QC system. The ρ_{5-6} plot for the first layer is shown in panel (d). In this system, as the chemical potential μ^* increases, the order parameter gradually decreases reaching a value of ~ 0.3 at $\mu_{tr}^* \sim 0.8$. Suddenly it drops to 0.017 and remains constant until bulk condensation. Similar behavior is observed at higher temperatures up to

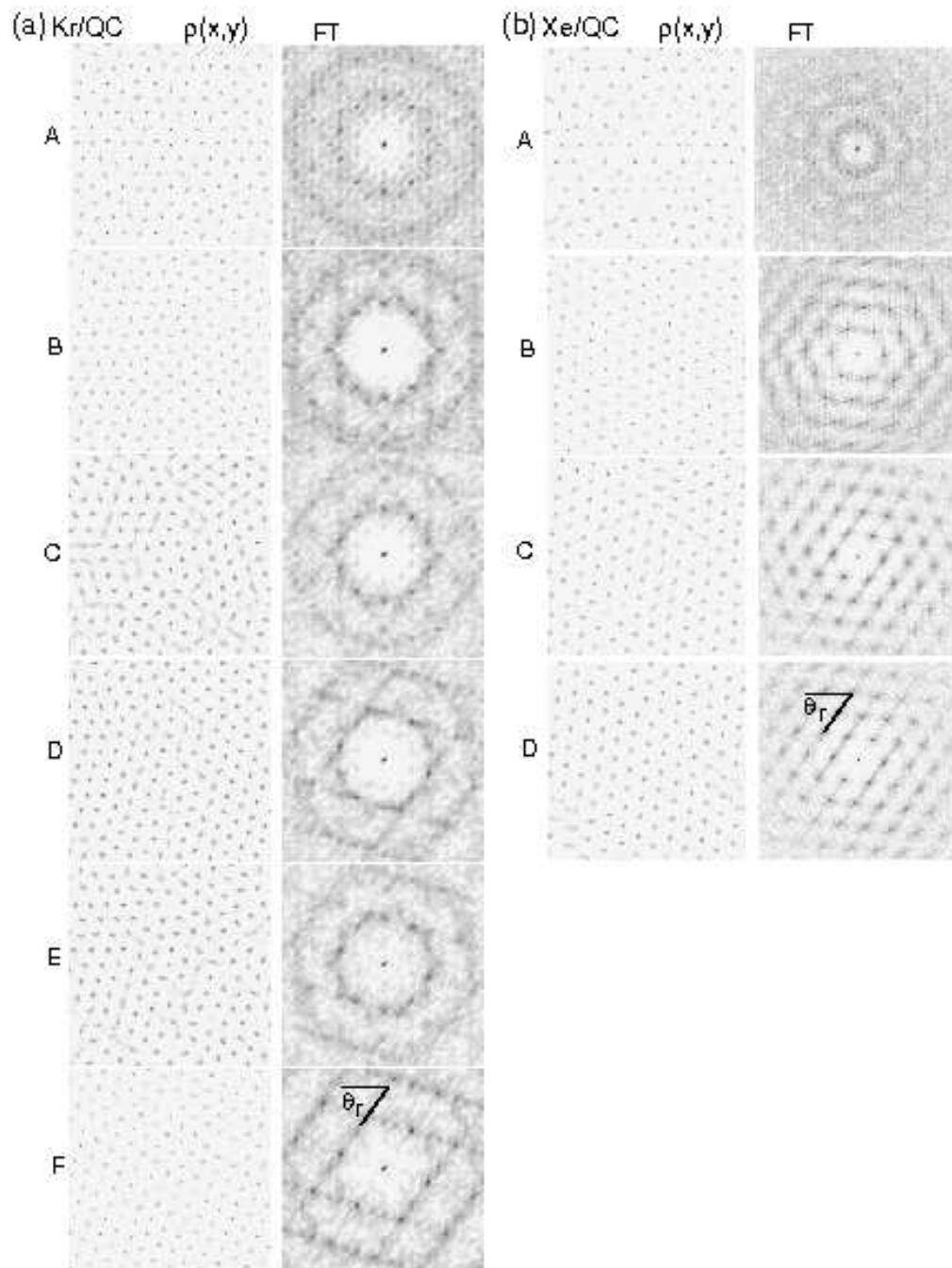


Figure 4. Density profiles and Fourier transforms of the outer layer at $T^* = 0.35$ for of Kr/QC ($T = 59.6$ K) and Xe/QC ($T = 77$ K), corresponding to points (A) through (F) of figure 2.

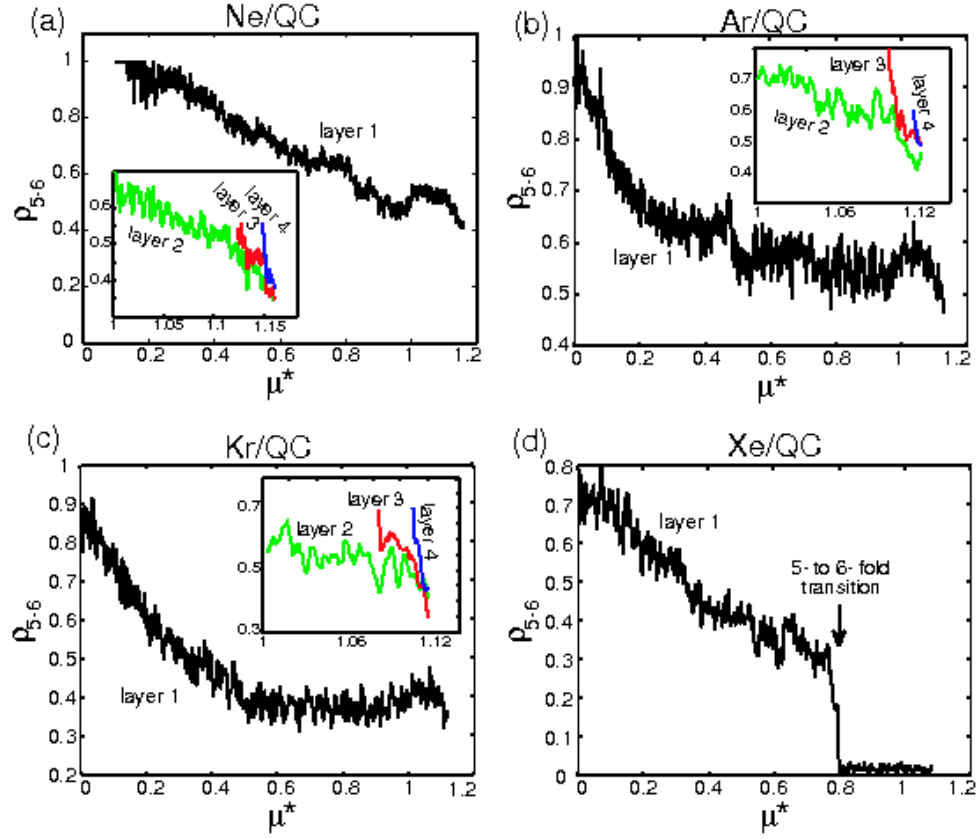


Figure 5. (color online). Order parameters, ρ_{5-6} , as a function of normalized chemical potential, μ^* , (as defined in the text) at $T^* = 0.35$ for the first four layers of (a) Ne, (b) Ar, (c) Kr, and for the first layer of Xe (d) adsorbed on the quasicrystal. A sudden drop of the order parameter in Xe/QC to a constant value of ~ 0.017 at $\mu^* \sim 0.8$ indicates the existence of a first-order structural transition from fivefold to sixfold in the system.

$T=140$ K ($T^*=0.63$). This is a clear indication of a five to sixfold ordering transition, as the first layer has undergone a transformation to an almost perfect triangular lattice. In addition, the transition has been found to have temperature-dependent critical chemical potential ($\mu_{tr}(T)$), and to be first order with associated latent heat[24, 25].

4. Discussion

In Section 3.1 we have briefly discussed how the density increase of each layer ($\Delta\rho_N$) is affected by the size of the adsorbate (σ_{gg}). In addition, since the corrugation of the potential depends also on the gas-gas interaction (ϵ_{gg}), the latter quantity could *a priori* have an effect on the density increase. To decouple the effects of σ_{gg} and ϵ_{gg} on $\Delta\rho_N$ we calculate $\Delta\rho_N$ while keeping one parameter constant, σ_{gg} or ϵ_{gg} , and varying the other. For this purpose, we introduce two fictitious gases iNe⁽¹⁾ and dXe⁽¹⁾, which represent “inflated” or “deflated” versions of Ne and Xe, respectively (parameters are defined in

equations 9-12 and listed in tables 1 and 2). Then we perform four tests summarized as the following:

- (1) constant strength ϵ_{gg} , size σ_{gg} increases [$\text{Ne} \rightarrow \text{iNe}^{(1)}$]: $\Delta\rho_N$ reduces,
- (2) constant strength ϵ_{gg} , size σ_{gg} decreases [$\text{Xe} \rightarrow \text{dXe}^{(1)}$]: $\Delta\rho_N$ increases,
- (3) constant size σ_{gg} , strength ϵ_{gg} decreases [$\text{Xe} \rightarrow \text{iNe}^{(1)}$]: $\Delta\rho_N \sim \text{constant}$,
- (4) constant size σ_{gg} , strength ϵ_{gg} increases [$\text{Ne} \rightarrow \text{dXe}^{(1)}$]: enhanced agglomeration.

Figure 6 shows the adsorption isotherms at $T^*=0.35$ for Ne, iNe⁽¹⁾, Xe, and dXe⁽¹⁾ on the QC. By keeping the strength constant and varying the size of the adsorbates, tests 1 and 2 ($[\text{Ne} \rightarrow \text{iNe}^{(1)}]$ and $[\text{Xe} \rightarrow \text{dXe}^{(1)}]$), we find that we can reduce or increase the value of the density increase (when $\Delta\rho_N$ decreases the continuous growth tends to become stepwise and vice versa). These two tests indicate that the larger the size, the smaller the $\Delta\rho_N$. By keeping the size constant and decreasing the strength, test 3 ($[\text{Xe} \rightarrow \text{iNe}^{(1)}]$), we find that $\Delta\rho_N$ does not change appreciably. An interesting phenomenon occurs in test 4 where we keep the size constant and increase the strength ($[\text{Ne} \rightarrow \text{dXe}^{(1)}]$). In this test the growth of the film loses its step-like shape. We suspect that this is caused by an enhanced agglomeration effect as follows. Ne and dXe⁽¹⁾ have the same size which is the smallest of the simulated gases, allowing them to easily follow the substrate corrugation, in which case, the corrugation helps to bring adatoms closer to each other [32] (agglomeration effect). The stronger gas-gas self interaction of dXe⁽¹⁾ compared to Ne will further enhance this agglomeration effect, resulting in a less stepwise film growth of dXe⁽¹⁾ than Ne. As can be seen, dXe⁽¹⁾ grows continuously, suggesting a strong enhancement of the agglomeration. In summary, the last two tests (3 and 4) indicate that the effect of varying the interaction strength of the adsorbates (while keeping the size constant) is negligible on large gases but significant on small gases.

Strength ϵ_{gg} and size σ_{gg} of the adsorbates also affect the existence of the first-order transition (present in Xe/QC, but absent in Ne/QC, Ar/QC, and Kr/QC). Hence we perform the same four tests described before and observe the evolution of the order parameter. The results are the following:

- (1) constant strength ϵ_{gg} , size σ_{gg} increases [$\text{Ne} \rightarrow \text{iNe}^{(1)}$]: transition appears
- (2) constant strength ϵ_{gg} , size σ_{gg} decreases [$\text{Xe} \rightarrow \text{dXe}^{(1)}$]: transition disappears
- (3) constant size σ_{gg} , strength ϵ_{gg} decreases [$\text{Xe} \rightarrow \text{iNe}^{(1)}$]: transition remains
- (4) constant size σ_{gg} , strength ϵ_{gg} increases [$\text{Ne} \rightarrow \text{dXe}^{(1)}$]: remains no transition

The strength ϵ_{gg} has no effect on the existence of the transition (tests 3 and 4), which instead is controlled by the size of the adsorbates (tests 1 and 2). To further characterize such dependence, we add three additional fictitious gases with the same strength ϵ_{gg} of Xe but different sizes σ_{gg} . The three gases are denoted as dXe⁽²⁾, iXe⁽¹⁾, and iXe⁽²⁾ (the prefixes d- and i- stand for deflated and inflated, respectively). The interaction parameters, defined in the following equations, are listed in tables 1 and 2:

$$\{\epsilon_{gg}, D_{gs}, \sigma_{gg}\} [\text{dXe}^{(2)}] \equiv \{\epsilon_{gg}, D_{gs}, 0.95\sigma_{gg}\} [\text{Xe}], \quad (15)$$

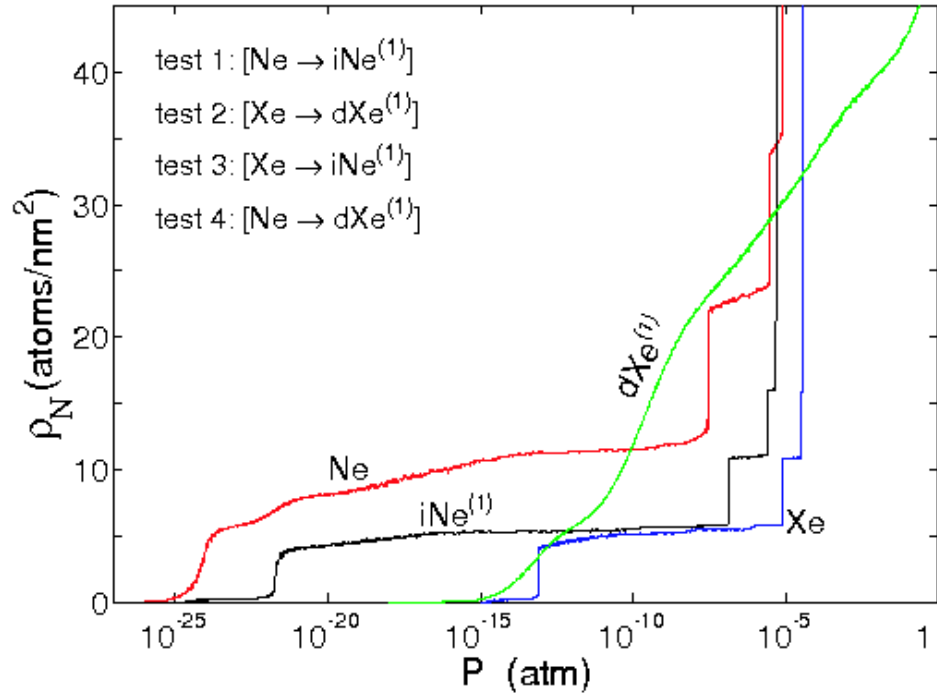


Figure 6. (color online). Computed adsorption isotherms for Ne, Xe, iNe⁽¹⁾, and dXe⁽¹⁾ on the quasicrystal at $T^*=0.35$. iNe⁽¹⁾ and dXe⁽¹⁾ are fictitious noble gases having potential parameters described in the text and in tables 1 and 2. The effect of varying the interaction strength of the adsorbates on the density increase $\Delta\rho_N$ (while keeping the size constant) is negligible on large gases but significant on small gases.

$$\{\epsilon_{gg}, D_{gs}, \sigma_{gg}\}[iXe^{(1)}] \equiv \{\epsilon_{gg}, D_{gs}, 1.34\sigma_{gg}\}[Xe], \quad (16)$$

$$\{\epsilon_{gg}, D_{gs}, \sigma_{gg}\}[iXe^{(2)}] \equiv \{\epsilon_{gg}, D_{gs}, 1.65\sigma_{gg}\}[Xe]. \quad (17)$$

Figure 7 shows the evolutions of the order parameter as a function of the normalized chemical potential for the first layer of dXe⁽²⁾, iNe⁽¹⁾, iXe⁽¹⁾, and iXe⁽²⁾ adsorbed on the QC at $T^*=0.35$. All these systems undergo a transition, except dXe⁽²⁾/QC, i.e. the transition occurs only in systems with $\sigma_{gg} \geq \sigma_{gg}[Xe]$ indicating the existence of a critical value for the appearance of the phenomenon. Furthermore, as σ_{gg} increases (iNe⁽¹⁾ \rightarrow iXe⁽¹⁾ \rightarrow iXe⁽²⁾), the transition shifts towards smaller critical chemical potentials.

The critical value of σ_{gg} can be related to the characteristic length of the QC by introducing a *gas-QC mismatch parameter* defined as

$$\delta_m \equiv \frac{k \cdot \sigma_{gg} - \lambda_r}{\lambda_r}. \quad (18)$$

where $k = 0.944$ is the distance between rows in a close-packed plane of a bulk LJ gas (calculated at $T = 0$ K with $\sigma = 1$ [39]), and λ_r is the characteristic spacing of the QC, determined from the momentum transfer analysis of LEED patterns [31] (our QC surface has $\lambda_r=0.381$ nm [31]). With such *ad hoc* definition, δ_m measures the mismatch between an adsorbed FCC[111] plane of adatoms and the QC surface. In table 4 we

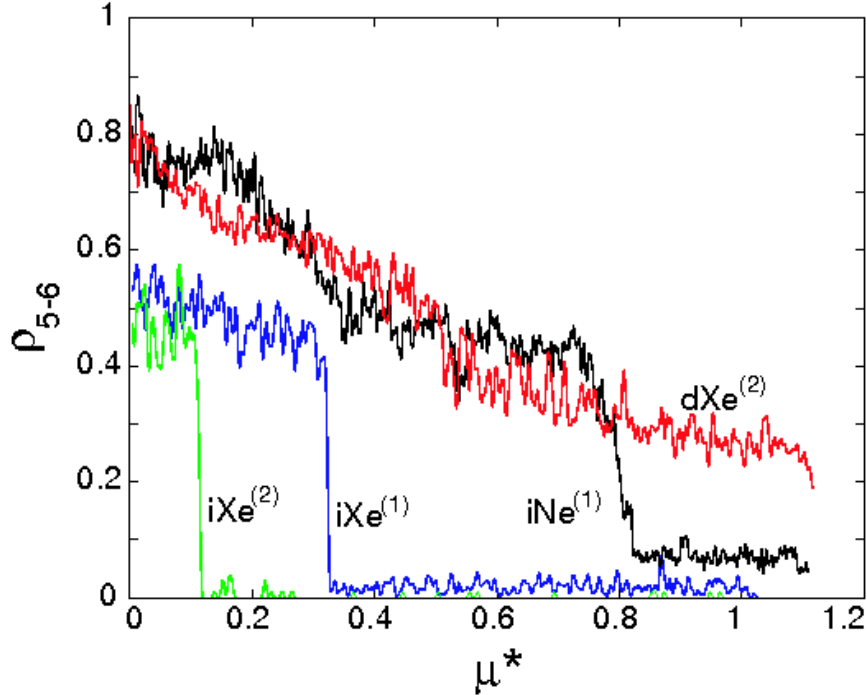


Figure 7. (color online). Order parameters as a function of normalized chemical potential (as defined in the text) for the first layer of $dXe^{(2)}$, $iNe^{(1)}$, $iXe^{(1)}$, and $iXe^{(2)}$ adsorbed on the quasicrystal at $T^* = 0.35$. A first-order fivefold to sixfold structural transition occurs in the last three systems, but not in $dXe^{(2)}$ /QC.

show that δ_m perfectly correlates with the presence of the transition in our test cases (transition exists $\Leftrightarrow \delta_m > 0$).

Table 4. Summary of adsorbed noble gases on the QC that undergo a first-order fivefold to sixfold structural transition and those that do not.

	δ_m	transition
Ne	-0.311	No
Ar	-0.158	No
Kr	-0.108	No
Xe	0.016	Yes
$iNe^{(1)}$	0.016	Yes
$dXe^{(1)}$	-0.311	No
$dXe^{(2)}$	-0.034	No
$iXe^{(1)}$	0.363	Yes
$iXe^{(2)}$	0.672	Yes

The definition of a gas-QC mismatch parameter is not unique. For example, one can substitute $k \cdot \sigma_{gg}$ with the first NN distance of the bulk gas, and λ_r with one of the following characteristic lengths: a) side length of the central pentagon in the potential plots in fig. 1 ($\lambda_s = 0.45\text{nm}$), b) distance between the center of the central pentagon and one of its vertices ($\lambda_c = 0.40\text{nm}$), c) $L = \tau \cdot S = 0.45\text{ nm}$, where $\tau = 1.618$ is the

golden ratio of the QC and $S = 0.243$ nm is the side length of the rhombic Penrose tiles [28]. Although there is no *a priori* reason to choose one definition over the others, the one that we select (equation 18) has the convenience of being perfectly correlated with the presence of the transition, and of using reference lengths commonly determined in experimental measurements (λ_r) or quantities easy to extract ($k \cdot \sigma_{gg}$).

In figure 1 we can observe that near the center of each potential there is a set of five points with the highest binding interaction (the dark spots constituting the central pentagons). A real QC surface contains an infinite number of these very attractive positions which are located at regular distances and with five fold symmetry. Due to the limited size and shape of the simulation cell, our surface contains only one set of these points. Therefore, it is of our concern to check if the results regarding the existence of the transition are real or artifacts of the method. We perform simulation tests by mitigating the effect of the attractive spots through a Gaussian smoothing function which reduces the corrugation of the original potential. The definitions are the following:

$$G(x, y, z) \equiv A_G e^{-(x^2+y^2+z^2)/2\sigma_G^2}, \quad (19)$$

$$V(z) \equiv \langle V(x, y, z) \rangle_{(x, y)}, \quad (20)$$

$$V_{mod}(x, y, z) \equiv V(x, y, z) \cdot [1 - G(x, y, z)] + V(z) \cdot G(x, y, z). \quad (21)$$

where $G(x, y, z)$ is the Gaussian smoothing function (centered on the origin and with parameters A_G and σ_G), $V(z)$ is the average over (x, y) of the original potential $V(x, y, z)$, and $V_{mod}(x, y, z)$ is the final smoothed interaction. An example is shown in figure 8(a) where we plot the minimum of the adsorption potential for a Ne/QC modified interaction (smoothed using $A_G = 0.5$ and $\sigma_G = 0.4$ nm). In addition, in panel (b) we show the variations of the minimum adsorption potentials along line $x = 0$ for the modified and original interactions (solid and dotted curves, respectively).

Using the modified interactions (with $A_G = 0.5$ and $\sigma_G = 0.4$ nm) we simulate all the noble gases of table 4. The results regarding the phase transition on modified surfaces do not differ from those on unmodified ones, confirming that the observed transition behavior is a consequence of competing interactions between the adsorbate and the whole QC substrate rather than just depinning of the monolayer epitaxially nucleated. Therefore, the simple criterion for the existence of the transition ($\delta_m > 0$) might also be relevant for predicting such phenomena on other decagonal quasicrystal substrates.

5. Conclusions

We have presented the results of GCMC simulations of noble gas films on QC. Ne, Ar, Kr, and Xe grow layer-by-layer at low temperatures up to several layers before bulk condensation. We observe interesting phenomena that can only be attributed to the quasicrystallinity and/or corrugation of the substrate, including structural evolution of the overlayer films from commensurate pentagonal to incommensurate triangular,

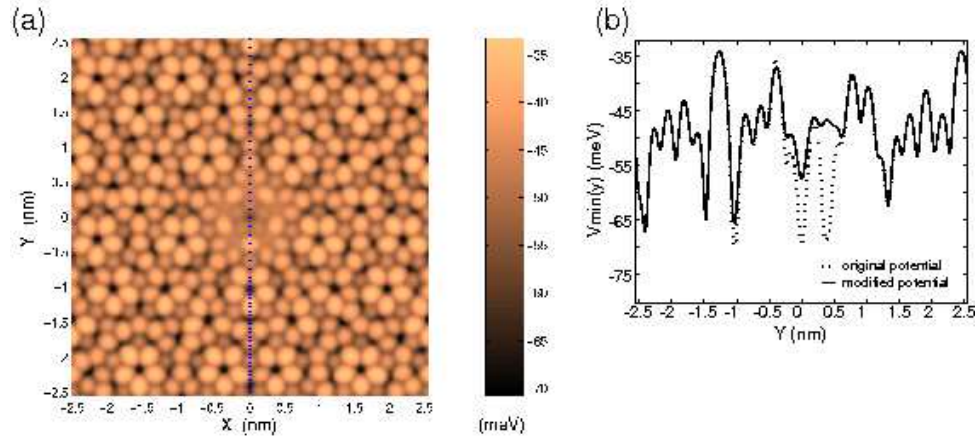


Figure 8. (color online). (a) The minimum of adsorption potential, $V_{min}(x, y)$, for Ne on a smoothed QC as described in the text. (b) The variations of the minimum adsorption potentials along the line at $x = 0$ shown in (a), for the modified and original interactions (solid and dotted curves).

substrate-induced alignment of the incommensurate films, and density increase in each layer with the largest one observed in the first layer and in the smallest gas. Two-dimensional quasicrystalline epitaxial structures of the overlayer form in all the systems only in the monolayer regime and at low pressure. The final structure of the films is a triangular lattice with a considerable amount of defects except in Xe/QC. Here a first-order transition occurs in the monolayer regime resulting in an almost perfect triangular lattice. The subsequent layers of Xe/QC have hexagonal close-packed structures. By simulating fictitious systems with various sizes and strengths, we find that the dimension of the noble gas, σ_{gg} , is the most crucial parameter in determining the existence of the phenomenon which is found only in systems with $\sigma_{gg} \geq \sigma_{gg}[\text{Xe}]$. The results of this study will be investigated in future experiments carried out in this laboratory, analogous to those already performed with Xe.

This work stimulates more comprehensive studies of adsorption heterogeneities on QC to understand the fundamental factors controlling the structure of single-element films by elucidating phenomena that are due exclusively to the quasiperiodicity of the substrate, as opposed to chemical interactions between the adsorbates and the surface.

Acknowledgments

We wish to acknowledge helpful discussions with L W Bruch, M Widom, A N Kolmogorov, C Henley, L Howle, D Rabson and R Trasca. We acknowledge the San Diego Supercomputer Center for computing time under Proposal Number MSS060002. This research was supported by NSF grant DMR-0505160.

References

- [1] Schick M 1981 *Progress in Surf. Sci.* **11** 245
- [2] Bruch L W, Cole M W and Zaremba E 1997 *Physical Adsorption* (Oxford: Oxford U P)
- [3] Sander L M and Hautman J 1984 *Phys. Rev. B* **29** 2171
- [4] Fairobent D K, Saam W F and Sander L M 1982 *Phys. Rev. B* **26** 179
- [5] Smith A R, Chao K-J, Niu Q and Shih C K 1996 *Science* **273** 226
- [6] Ebert P, Chao K-J, Niu Q and Shih C K 1996 *Phys. Rev. Lett.* **83** 3222
- [7] Grimm B, Hövel H, Pollmann M and Reihl B 1999 *Phys. Rev. Lett.* **83** 991
- [8] Leatherman G S and Diehl R D 1996 *Phys. Rev. B* **53** 4939
- [9] Leatherman G S, Karimi M, Vidali D and Diehl R D 1997 *Phys. Rev. B* **56** 6970
- [10] D'Amico K L, Moncton D E, Specht E D, Birgeneau R J, Nagler S E and Horn P M 1984 *Phys. Rev. Lett.* **53** 2250
- [11] Fain Jr S C, Chinn M D and Diehl R D 1980 *Phys. Rev. B* **21** 4170
- [12] Novaco A D and McTague J P 1977 *Phys. Rev. Lett.* **38** 1286
- [13] Tkatchenko A *Phys. Rev. B* 2006 **74** 035428
- [14] Noakes T C Q, Bailey P, Draxler M, McConville C F, Ross A R, Lograsso T A, Leung L, Smerdon J A and McGrath R 2006 *J. Phys.: Condens. Matt.* **18** 5017
- [15] Cai T, Ledieu J, McGrath R, Fournée, Lograsso T, Ross A and Thiel P 2003 *Surf. Sci.* **526** 115
- [16] Ledieu J, Hoeft J T, Reid D E, Smerdon J A, Diehl R D, Lograsso T A, Ross A R and McGrath R 2004 *Phys. Rev. Lett.* **92** 135507
- [17] McGrath, Ledieu J, Cox E J and Diehl R D 2002 *J. Phys.: Condens. Matt.* **14** R119
- [18] Fournée V, Sharma H R, Shimoda M, Tsai A P, Unal B, Ross A R, Lograsso T A and Thiel P A 2005 *Phys. Rev. Lett.* **95** 155504
- [19] Franke K J, Sharma H R, Theis W, Gille P, Ebert Ph and Rieder K H 2002 *Phys Rev. Lett.* **89** 156104
- [20] Bolliger B, Dmitrienko V E, Erbudak M, Lüscher R and Nissen H -U 2001 *Phys. Rev. B* **63** 052203
- [21] Fournée V, Cai T C, Ross A R, Lograsso T A, Evans J W and Thiel P A 2003 *Phys. Rev. B* **67** 033406
- [22] Curtarolo S, Setyawan W, Ferralis N, Diehl R D and Cole M W 2005 *Phys. Rev. Lett.* **95** 136104
- [23] Diehl R D, Ferralis N, Pussi K, Cole M W, Setyawan W and Curtarolo S 2006 *Phil. Mag.* **86** 863
- [24] Setyawan W, Ferralis N, Diehl R D, Cole M W and Curtarolo S 2006 *Phys. Rev. B* **74** 125425
- [25] R D Diehl, W Setyawan, N Ferralis, R A Trasca, M W Cole and S Curtarolo 2006 *submitted to Phil. Mag.*
- [26] Frenkel D and Smith B 2002 *Understanding Molecular Simulations: From Algorithms to Application* (New York: Academic)
- [27] Allen M P and Tildesley D J 1987 *Computer Simulation of Liquids* (Oxford: Oxford U P)
- [28] Ferralis N, Pussi K, Gierer M, Cox E J, Ledieu J, Fisher I R, Jenks C J, Lindroos M, McGrath R and Diehl R D 2004 *Phys. Rev. B* **69** 153404
- [29] Pussi K, Ferralis N, Mihalkovic M, Widom M, Curtarolo S, Gierer M, Jenks C J, Fisher I R and Diehl R D 2006 *Phys. Rev. B* **73** 184203
- [30] Bojan M J, Stan G, Curtarolo S, Steele W A and Cole M W 1999 *Phys. Rev. E* **59** 864
- [31] Ferralis N, Diehl R D, Pussi K, Lindroos M, Fisher I R and Jenks C J 2004 *Phys. Rev. B* **69** 075410
- [32] Trasca R A, Ferralis N, Diehl R D and Cole M W 2004 *J. Phys.: Condens. Matt.* **16** S2911
- [33] Reference [2]: p. 67.
- [34] Zeppenfeld P 2001 *Physics of Covered Surfaces* in *Landolt-Bornstein New Series Group III* **42** ed Bonzel H P (Berlin: Springer) p 67
- [35] Vidali G, Ihm G, Kim H -Y and Cole M C 1991 *Surf. Sci. Rep.* **12** 135
- [36] Curtarolo S, Stan G, Cole M W, Bojan M J and Steele W A 1999 *Phys. Rev. E* **59** 4402
- [37] Curtarolo S, Stan G, Bojan M J, Cole M W and Steele W A 2000 *Phys. Rev. E* **61** 1670

- [38] Crawford R K 1977 *Rare Gas Solids* **2** ed Klein M L and Venables J A (London: Academic) p 663
- [39] Bruch L W, Cohen P I and Webb M B 1976 *Surf. Sci.* **59** 1